

Companion Shocking Fits to the 2018 ZTF Sample of SNe Ia Are Consistent with Single-Degenerate Progenitor Systems

J. BURKE,^{1,2} D. A. HOWELL,^{1,2} D. J. SAND,³ AND G. HOSSEINZADEH³

¹*Las Cumbres Observatory, 6740 Cortona Dr, Suite 102, Goleta, CA 93117-5575, USA*

²*Department of Physics, University of California, Santa Barbara, CA 93106-9530, USA*

³*Steward Observatory, University of Arizona, 933 North Cherry Avenue, Tucson, AZ 85721-0065, USA*

(Received XXX; Revised XXX; Accepted XXX)

Submitted to ApJL

ABSTRACT

The early lightcurves of Type Ia supernovae (SNe Ia) can be used to test predictions about their progenitor systems. If the progenitor system consists of a single white dwarf in a binary with a Roche-lobe-overflowing non-degenerate stellar companion, then the SN ejecta should collide with that companion soon after the explosion and get shock-heated, leaving an early UV excess in the lightcurve. This excess would only be observable for events with favorable viewing angles, $\sim 10\%$ of the time. We model the 2018 ZTF sample of 127 SNe Ia using companion shocking models, and recover an observed early excess rate of $12.0 \pm 3.6\%$, consistent both with several other rates calculated throughout the literature, and with the expectation that SNe Ia predominantly occur in single-degenerate systems. We observe early excesses only in spectroscopically normal SNe Ia, in contradiction to the claim that such excesses occur more frequently in overluminous SNe Ia. We also show that the detection of early excesses can be methodology-dependent. We encourage the observation of large samples of SNe Ia with high-cadence multiwavelength early data in order to test the statistical predictions of SN Ia progenitor models, and we also encourage the refinement of existing models.

Keywords: supernovae

1. INTRODUCTION

Type Ia supernovae (SNe Ia) come from exploding white dwarfs (WDs). This statement is uncontroversial and has been understood for decades (Hoyle & Fowler 1960), but almost every detail of the progenitor system and explo-

sion mechanism is the subject of active research. What mass are the WDs when they explode? Do they need to accrete mass up to the Chandrasekhar limit, or, as some models predict (e.g. Polin et al. 2019; Shen et al. 2021), can they explode at sub-Chandrasekhar masses? Where does the explosion start? Does it begin roughly at the center of the WD (Khokhlov 1991), or does it begin in a surface layer of accreted He which causes the underlying WD to detonate

Corresponding author: J. Burke (he, him)
jburke@lco.global

(Polin et al. 2019)? How do the WDs gain enough mass to explode? Are they in a binary system with a Roche-lobe-overflowing non-degenerate stellar companion (referred to as the “single-degenerate” case; Hoyle & Fowler 1960), or does the primary WD tidally disrupt a less massive secondary WD (the “double-degenerate” case; Iben & Tutukov 1984)? These and many other questions have yet to be definitively answered.

SNe Ia have standardizable lightcurves, especially around peak (see e.g. Riess et al. 1998; Perlmutter et al. 1999; Phillips et al. 1999). But their early lightcurves, within a few days of explosion, are much less homogeneous and can contain observational signatures which reveal information about their progenitor systems. One such signature was predicted in Kasen (2010): in the single-degenerate case, as the SN ejecta collide with a nondegenerate companion they will get shock-heated, resulting in early UV excesses which should be observable for binaries with favorable viewing angles ($\sim 10\%$ of events). After these early UV excesses were predicted they (or similar effects) have subsequently been observed in a small number of objects: SN 2012cg (Marion et al. 2016), iPTF14atg (Cao et al. 2015), SN 2016jhr (aka MUSSES1604D, Jiang et al. 2017), iPTF16abc (Miller et al. 2018), SN 2017cbv (Hosseinzadeh et al. 2017), SNe 2017erp and 2018yu (Burke et al. 2022), SN 2019yvq (Miller et al. 2020a; Siebert et al. 2020; Tucker et al. 2021; Burke et al. 2021), and SN 2021aefx (Ashall et al. 2022; Hosseinzadeh et al. 2022). Some other objects have early excesses, but without the color information needed to determine their temperature, such as SN 2018oh (Li et al. 2019; Dimitriadis et al. 2019; Shappee et al. 2019) and SN 2020hvf (Jiang et al. 2021), and still others (SN 2018aoz; Ni et al. 2022a,b) have early color evolution which can differ by more than a magnitude from a typical SN Ia.

Most of the above objects were modeled with companion interaction models, but there are other physical models which can produce early excesses. “Double-detonation” models, where the WD builds up a layer of He on its surface until the He detonates, driving a shockwave into the WD causing it to detonate in turn, can also produce a range of early lightcurve behavior due to the presence of extra radioactive products in the outer ejecta (see Sim et al. 2012; Polin et al. 2019). Models which vary the distribution of ^{56}Ni , which powers SN Ia lightcurves (Pankey 1962), can also produce a range of early behavior, including early bumps (Magee et al. 2018; Magee & Maguire 2020; Magee et al. 2020). Both classes of models produce extra radioactive material in the outer ejecta, resulting in some similar effects (e.g. “red bumps” at early times), which makes them potentially difficult to distinguish for near-Chandrasekhar-mass WDs.

Recently, Burke et al. (2022) examined a sample of 9 SNe Ia with exemplary high-cadence multiwavelength early data. Overall the paper favored companion interaction models to explain both objects which exhibit an early excess, and those that do not. The sample was constructed using a set of criteria to make it as unbiased as possible, and contained one object with a strong early excess and two others with weaker excesses. Based on the distributions of early excess strengths and best-fit viewing angles, that paper concluded that there was not enough evidence to disprove the null hypothesis, i.e. that all SNe Ia come from single-degenerate progenitor systems.

In this paper we will be focusing solely on companion shocking models to explain early excesses. We do not claim that the models can perfectly explain every aspect of the dataset: we refer to the discussion section of Burke et al. (2022) for an explicit list of their pros and cons. Perhaps the strongest point against them is the

lack of H observed in the nebular spectra of SNe Ia (see e.g. Sand et al. 2019; Tucker et al. 2020), even though the ejecta-companion interaction should strip H from a non-degenerate companion (Botyánszki et al. 2018; Dessart et al. 2020). They also struggle to fit UV data: even though the process of shock heating should make the early excess strongest in the UV, the models consistently overpredict the UV flux (see e.g. Hosseinzadeh et al. 2017, 2022). Keeping these caveats in mind (and again, for a more in-depth discussion we refer to Burke et al. 2022), we nevertheless favor the models and use them to investigate the sample of SNe Ia presented here.

This paper follows very similar methodology to Burke et al. (2022), but applied to a different sample of SNe Ia. The sample here has an order of magnitude more objects but limited multi-band information when compared to Burke et al. (2022), making this a complementary analysis. In Section 2 we briefly describe our data and sample, and in Section 3 we describe the companion interaction models we use to fit the data. We show and discuss the results of the fits in Section 4, before concluding in Section 5.

2. DATA AND SAMPLE

The full dataset in this paper comes from Yao et al. (2019), so we refer to that paper for details of its acquisition and reduction. The data come from the ZTF survey (Bellm et al. 2019), and the dataset has many advantages: the large number of objects (127); the uniform inclusion of non-detections; and the high cadence of coverage, with some objects being observed not only nightly, but revisited six times per night (thrice in g and thrice in r). The primary downside of the dataset is that it is in only two filters, g and r , which strongly limits the number of filter combinations which can be used to determine color/temperature (compare e.g. the $UBVgri$ data used in Burke et al. 2022).

To obtain the data, we simply downloaded the digital version of Table 5 of Yao et al. (2019), which is a FITS file containing the full dataset in flux space. We convert to magnitude space following Equations 7–10 of that paper.

The sample was introduced in a series of three papers: Paper I (Yao et al. 2019) described the overall data reduction method and the properties of the sample itself; Paper II (Miller et al. 2020b) modeled the rising lightcurves of the sample to infer rise times; and Paper III (Bulla et al. 2020) analyzed the sample’s color evolution. Again, we refer to Yao et al. (2019) for a full description of the sample. In short, the sample contains 127 SNe Ia. All objects have observations earlier than at least 10 rest-frame days before maximum light, and 50 of the objects have detections earlier than 14 rest-frame days before peak. The median redshift of the sample is 0.076. Though we focus on photometry here, Yao et al. (2019) also discusses the spectroscopic classifications of the objects: 107 objects are “normal” SNe Ia (including the 25 SNe listed in the paper as “normal*,” i.e. tentatively classified as normal), 10 objects are 99aa-likes (including three tentative classifications), four objects are super-Chandrasekhar SNe Ia (including two tentative classifications), three are 91T-likes (including two tentative classifications), one is an 86G-like, one is an 02cx-like, and one is a Ia-CSM. We again refer to Yao et al. (2019) for details of the classifications, and also to Taubenberger (2017) for a discussion of the various different subtypes of SNe Ia.

3. MODELS

3.1. Initial Parameter Measurements

Following Burke et al. (2022), we utilize the Python package `SNooPy` (Burns et al. 2011) to measure several necessary quantities for the objects. We do `SNooPy` fits using the default `EBV_model` and the `fitMCMC()` procedure, enforcing $R_{V,host} = 3.1$. We impose a uniform

prior on `EBVhost` ranging from 0 to 1. We limit the data to the epochs relevant for `SNooPy` models, i.e. -10 to $+50$ days from peak (using MJD_{peak} as measured by Yao et al. 2019). We visually inspect fits to ensure that they are reasonable. We adopt the `SNooPy` values of distance moduli and host extinction for all objects throughout our analysis. We convert each object’s $E(B - V)$ (Milky Way + host) to per-filter extinction values using the Schlafly & Finkbeiner (2011) recalibration of the Schlegel et al. (1998) dust maps, accessed by the Python package `extinction` (Barbary 2016).

We also use `SNooPy` to measure K-corrections for the data, similar to Bulla et al. (2020). The way that `SNooPy` fits SN Ia lightcurves already involves K-corrections, making them straightforward to extract from the fits. This method of K-correction is the largest deviation from the methodology of Burke et al. (2022), which otherwise this paper follows quite closely. The sample of Burke et al. (2022) was low redshift ($z < 0.01$), so any K-correction would both be small and (as is inherent in doing K-corrections) would rely on assumptions about the underlying SED, even though those assumptions could be incorrect for objects with early excesses since their early spectra differ from SNe Ia without excesses (see e.g. Marion et al. 2016; Hosseinzadeh et al. 2017; Burke et al. 2021). Due to the much higher redshift of the sample here (median redshift 0.076) we deemed K-corrections necessary, since the models described in Section 3.2 rely on accurate absolute magnitudes both to compare to the rest-frame g and r template lightcurves and to compare to the strengths of any early excesses.

3.2. Companion Shocking Models

3.2.1. Description of models

Our models are similar to the ones used in Burke et al. (2022) (along with Hosseinzadeh et al. 2017 and Hosseinzadeh et al. 2022, and

to some extent those in Dimitriadis et al. 2019 and Miller et al. 2020a). They make use of the `lightcurve_fitting` Python package (Hosseinzadeh 2019), which performs MCMC fits using the `emcee` package (Foreman-Mackey et al. 2013). The model consists of two components: a template lightcurve from `SiFTO` (Conley et al. 2008) which is scaled and stretched to maximize overlap with the data, to which is added a blackbody component (which can dominate at early times) representing a companion shock interaction based on the analytical formulae from Kasen (2010). As in Burke et al. (2022) we add a parameter to represent the viewing angle, implemented as a multiplicative factor on the shock component following the semi-analytic formulation of Brown et al. (2012).

This results in a total of six parameters:

1. a , the companion separation of the shock component
2. t_{max} , the time of B -band maximum light for the stretch component
3. s , the stretch applied to the stretch component
4. r_r , a factor on the r -band flux of the stretch component
5. θ , the viewing angle (which determines a multiplicative factor on the shock component)
6. σ , a multiplicative factor on the errors of the data to account for error underestimation.

The models are identical to those used in Burke et al. (2022), except for the fact that two parameters used in that paper are excluded because they affect only non- gr data and are thus irrelevant for the dataset here. We refer to that paper for a more detailed description of the models – the two differences here are the slightly fewer parameters and the fact that we do the fits on

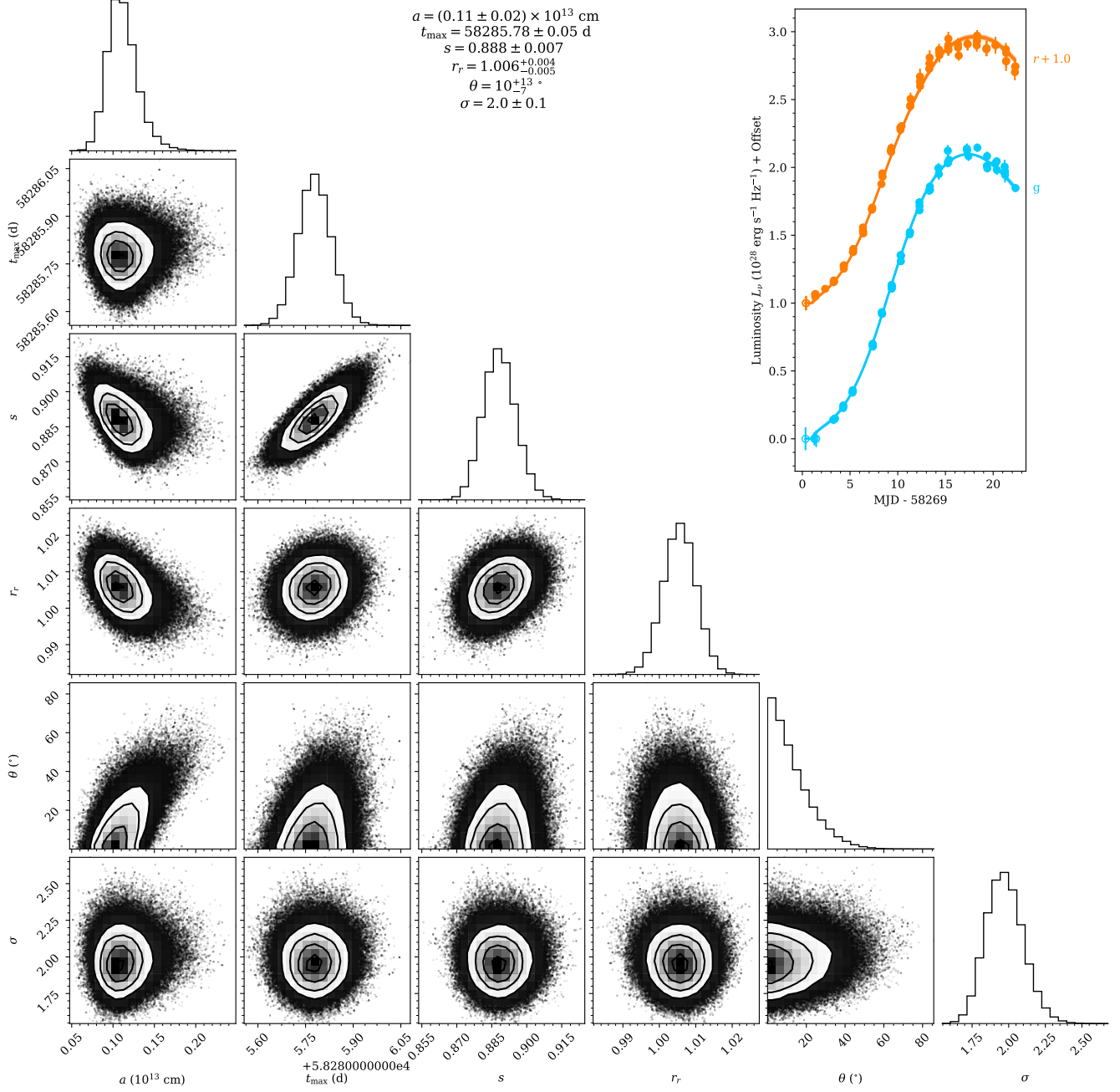


Figure 1. Corner plot of the model described in Section 3.2 for ZTF18aaxsioa, one of the objects we identify as having an early excess due to the fact that its posterior distribution of the θ parameter is peaked to $\theta = 0^\circ$. The inset data show the extremely high cadence and useful non-detections (first epoch shown, unfilled circles) typical of the sample.

the K-corrected data. We also refer to the discussion section of that paper for an explicit list of the pros and cons of the model, including various simplifying assumptions it makes.

A corner plot for an object we identify as having an early excess is shown in Figure 1.

3.2.2. Is It Valid to Use Just gr Data in Companion Shocking Models?

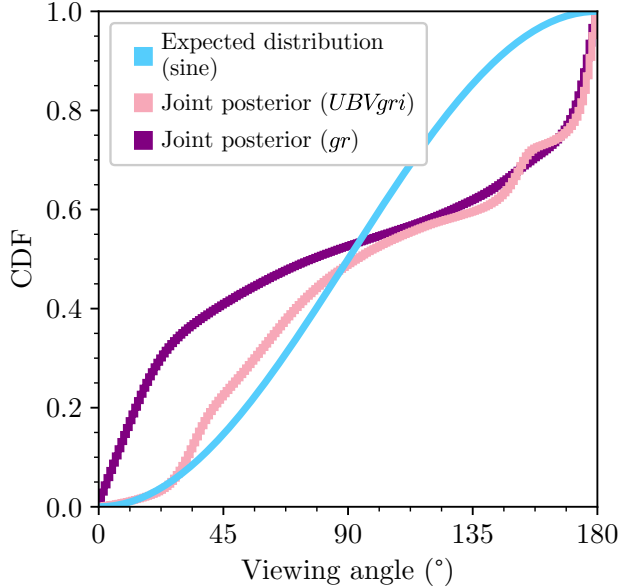


Figure 2. Joint viewing angle posteriors for the sample modeled in Burke et al. (2022), which markedly change from the result presented in that paper (the pink line) when the lightcurves are limited to just *gr* data (the purple line). We conclude that these models can still be used to detect early excesses in *gr* data, as objects exhibiting early excesses converge to low viewing angles, but the models shouldn’t be used to measure physical parameters. It also means that the K-S test method used in Burke et al. (2022) is no longer applicable for *gr* data alone.

Most of the literature using this style of modeling has access to highly multiwavelength datasets (see Burke et al. 2022 for the most direct comparison, but also Cao et al. 2015; Hosseinzadeh et al. 2017; Dimitriadis et al. 2019; Miller et al. 2020a; Burke et al. 2021; Hosseinzadeh et al. 2022). The wavelength coverage is often *UBVgri*, but sometimes extends further into the UV with data from the Neil Gehrels Swift Observatory (Swift; Gehrels et al. 2004). The temperature of the early data, accessed through different filter/color combinations, is a critical parameter implicitly measured in the models, making it natural to ask: is it valid to use only *gr* data with these models?

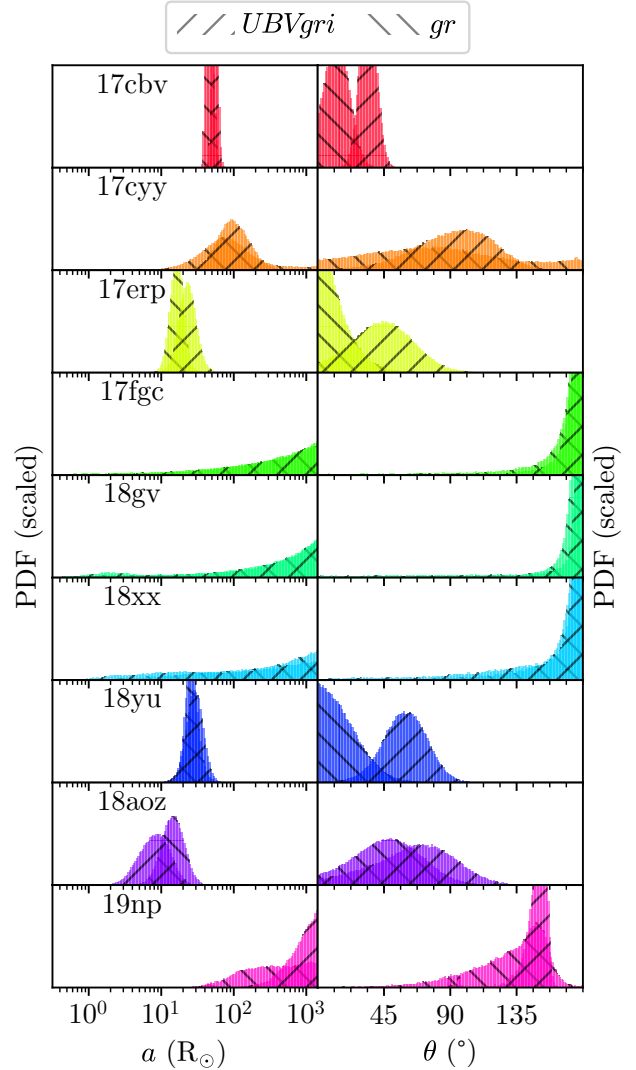


Figure 3. The per-object posteriors of the sample presented in Burke et al. (2022), which change depending on whether we use the object’s *UBVgri* dataset (as done in that paper) or just its *gr* data (as we do for the sample presented here). The three objects identified in that paper as having early excesses (SNe 2017cbv, 2017erp, and 2018yu) have best-fit viewing angles which shift towards $\theta = 0$ when the data are limited to *gr*.

To summarize the answer to that question: these models can still detect early excesses using only *gr* data, but they should not be used to measure physical parameters.

To see why this is the case, we reexamine the objects modeled in [Burke et al. \(2022\)](#), limiting the data from *UBVgri* down to *gr*. One result from that paper had to do with the joint MCMC posteriors of the θ parameter from the nine objects in that sample, where, when comparing the joint posterior to the expected distribution of viewing angles if all SNe Ia arose from single-degenerate systems, there was not enough evidence to disprove that null hypothesis.

Figure 2 shows the joint viewing angle posterior both as it was presented in that paper (the pink line), and when the data are limited to just *gr* (the purple line). This behavior is shown per-object in Figure 3, for both the θ and a posteriors. Looking at the figures, it’s clear that objects which have no detectable excess have still converged to having their maximum likelihood at $\theta = 180^\circ$, as they did in the *UBVgri* models (see SNe 2017fgc, 2018gv, and 2018xx in Figure 3). However, the three objects with detectable excesses (SNe 2017cbv, 2017erp, and 2018yu) now have a maximum likelihood closer to $\theta = 0^\circ$ in the *gr* fits.

This has three implications when the data are limited to *gr*. One is that the best-fit values of the two relevant physical parameters (i.e. θ and a) should not fully be believed: for example, even though the viewing angles seem to have converged nicely for the *gr* models, there is a systematic offset from the best-fit *UBVgri* values for the three objects with early excesses (SNe 2017cbv, 2017erp, and 2018yu). Their best-fit companion separations are also systematically lower, though at lower significance. However, even though the *gr* models shouldn’t be used to measure physical parameters, they can still be used to detect early excesses. Early excesses are still present in the data, regardless of filter (see Figure 3 of [Burke et al. 2022](#)), and will manifest as θ posteriors which peak towards low viewing angles. Lastly,

it also means that the K-S test done in [Burke et al. \(2022\)](#) to compare the joint viewing angle posterior to the null hypothesis is no longer applicable, since the per-object posteriors have changed significantly.

4. RESULTS

4.1. *Early Excess Rate*

In [Burke et al. \(2022\)](#), SNe were classified as having an early excess if they met three criteria: (1) if the object had data within five rest-frame days of inferred first light (the typical epochs for an early excess in [Kasen 2010](#)), (2) if the best-fit viewing angle was less than 90° , and (3) if the residuals with respect to the stretch template showed a systematic which was representative of an early-but-fading shock component (i.e. if they showed an initial discrepancy of $>5\sigma$ which decreased over time). We use similar criteria here: we keep criterion (1) unchanged; following the results of Section 3.2.2 we change criterion (2) to a best-fit $\theta \leq 45^\circ$; and we loosen the requirement of criterion (3) due to the lower S/N of the dataset, although such a pattern is still obvious for some objects.

Using the above criteria, we identify 11 objects with early excesses in our sample. Table 1 lists the best-fit parameters and some object properties for these 11 SNe. We have split the objects into tiers based on visual inspection of their fits and residuals (see Figure 5 and surrounding discussion). Since the sample contains 127 SNe in total, these 11 objects naïvely represents 8.7% of the total sample, although as we will discuss more shortly, the intrinsic rate of early excesses is slightly higher due to the low S/N of early data potentially obscuring some excesses.

Figure 4 shows the best-fit model and residuals for a single object which we identify as having an early excess (ZTF18aaxsioa, the same object shown in Figure 1). The distinctive pattern in the residuals with respect to the stretch tem-

ZTF18	a (R_{\odot})	t_{\max} (MJD)	s	r_r	θ ($^{\circ}$)	σ	IAU	z	Subtype
Gold tier									
aaxsioa	$15.8^{+2.7}_{-2.3}$	$58285.78^{+0.05}_{-0.05}$	$0.888^{+0.007}_{-0.007}$	$1.006^{+0.004}_{-0.005}$	10^{+13}_{-7}	$1.97^{+0.13}_{-0.12}$	cfa	0.0315	normal*
abcflnz	$9.4^{+1.5}_{-1.4}$	$58304.78^{+0.08}_{-0.08}$	$0.962^{+0.008}_{-0.007}$	$0.969^{+0.004}_{-0.004}$	6^{+9}_{-5}	$2.03^{+0.08}_{-0.07}$	cuw	0.0273	normal
Silver tier									
absuxz	34^{+17}_{-11}	$58376.82^{+0.20}_{-0.19}$	$0.860^{+0.024}_{-0.018}$	$0.987^{+0.014}_{-0.014}$	31^{+47}_{-23}	$1.15^{+0.13}_{-0.11}$	gfe	0.0649	normal
abxxssh	47^{+28}_{-15}	$58396.54^{+0.22}_{-0.19}$	$1.077^{+0.027}_{-0.022}$	$0.902^{+0.013}_{-0.014}$	27^{+34}_{-19}	$1.49^{+0.12}_{-0.11}$	gvj	0.0782	normal
aavrwhu	$31.5^{+8.7}_{-7.5}$	$58275.29^{+0.13}_{-0.13}$	$1.090^{+0.019}_{-0.017}$	$0.967^{+0.006}_{-0.007}$	15^{+22}_{-11}	$1.42^{+0.13}_{-0.11}$	bxo	0.062	normal
abfhryc	$15.9^{+6.9}_{-4.2}$	$58322.39^{+0.09}_{-0.08}$	$0.980^{+0.010}_{-0.009}$	$1.009^{+0.005}_{-0.005}$	25^{+27}_{-18}	$1.93^{+0.13}_{-0.12}$	dhw	0.0323	normal
Bronze tier									
aawjywv	38^{+19}_{-12}	$58270.85^{+0.18}_{-0.17}$	$0.855^{+0.024}_{-0.020}$	$0.962^{+0.015}_{-0.016}$	30^{+40}_{-22}	$2.02^{+0.19}_{-0.16}$	ccj	0.0509	normal*
aaqcozd	170^{+67}_{-25}	$58253.02^{+0.11}_{-0.11}$	$0.825^{+0.020}_{-0.015}$	$0.863^{+0.019}_{-0.015}$	37^{+40}_{-25}	$0.92^{+0.09}_{-0.08}$	bjc	0.0732	normal
abdfazk	94^{+53}_{-23}	$58306.60^{+0.22}_{-0.20}$	$0.906^{+0.032}_{-0.025}$	$0.924^{+0.019}_{-0.017}$	43^{+49}_{-29}	$1.17^{+0.11}_{-0.10}$	dbe	0.084	normal
abimsyv	55^{+28}_{-19}	$58333.03^{+0.19}_{-0.18}$	$1.003^{+0.021}_{-0.020}$	$0.915^{+0.012}_{-0.012}$	41^{+31}_{-26}	$1.16^{+0.07}_{-0.06}$	eni	0.088	normal*
aazsabq	$12.1^{+4.8}_{-3.3}$	$58293.40^{+0.10}_{-0.10}$	$0.891^{+0.012}_{-0.011}$	$1.006^{+0.006}_{-0.006}$	21^{+26}_{-15}	$1.38^{+0.09}_{-0.08}$	crn	0.06	normal

Table 1. Values of the best-fit parameters and some object properties for the 11 SNe we identify as having early excesses. The “ZTF18” column is the ZTF name (with the “ZTF18-” excluded for space). The next six columns are the best-fit parameters from the models described in Section 3.2. Lastly we give the IAU name (again excluding the “SN 2018-” for space), the redshift, and the classification as listed in Yao et al. (2019). We have split the objects into tiers based on visual inspection of the fits and their residuals (see Figure 5 and surrounding discussion).

plate (diamonds), where their discrepancy diminishes over time, is characteristic of an early-but-fading shock component (see Figure 3 of Burke et al. 2022).

The sample modeled in Burke et al. (2022) consisted of nine objects, three of which had early excesses: that paper therefore calculated an early excess rate from simple Poissonian statistics of $33 \pm 19\%$. However, the objects in that paper were extremely low-redshift ($z < 0.01$), and all objects were detected well above the telescopes’ limiting magnitudes within five days of inferred first light. (“First light” in this context being the time when the SN flux is first detectable, which is not necessarily the same as when the explosion occurred due to “dark phases” in SNe Ia when the radiation has not yet diffused out of the ejecta – see Piro & Nakar 2013, where this is discussed in more detail.)

Burke et al. (2022) assumed that any potential early excesses would be revealed by the data. The sample here is significantly different: it is much higher redshift (median redshift of 0.076), resulting in lower average signal-to-noise (S/N) in the crucial earliest epochs.

This lower S/N could serve to obscure weak early excesses hiding in the data. For instance, in this sample only 81% of the objects (103 out of 127) are detected at all within 5 rest-frame days of inferred first light. Table 2 shows the results of imposing different S/N cuts on the early data of the sample, e.g. only considering objects which have a $>10\sigma$ detection with 5 days of first light. Each S/N cut leaves some total number of objects, and also some subset of the early-excess objects, from which an early excess rate can be calculated. The 30σ cut leaves a sample extremely similar to the one in Burke et al.

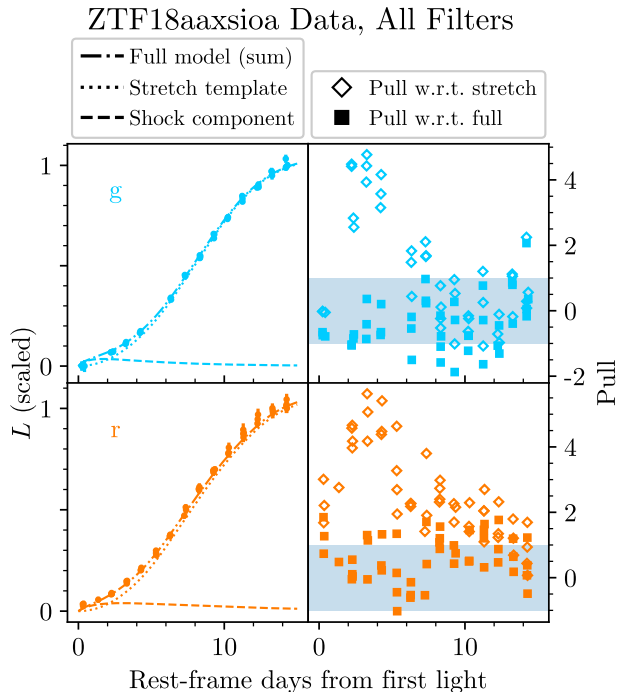


Figure 4. The best-fit model and residuals for ZTF18aaxsioa, an object with an early excess. The left panels show the per-filter data and the two components of the model: the stretched template (dotted line) and the shock component (dashed), which are added together to the full model. The right panels show the residuals with respect to both the full model (filled squares) and the stretched template (empty diamonds), where the signature of the early excess is obvious (initial discrepancy which vanishes over time). “Pull” is defined as the number of standard deviations a data point is away from the relevant model, divided by the best-fit σ value – the majority of square points should cluster within one standard deviation of zero (the grey shaded box), which they do.

(2022): that paper had an early excess rate of 3 out of 9 objects ($33 \pm 19\%$), and limiting the sample here to SNe with a 30σ detection in the epochs where an early excess could be detected yields a rate of 2 out of 9 objects ($22 \pm 16\%$). We thus believe that the sample here is identical to the sample of Burke et al. (2022), except at higher redshift and observed in fewer bands. As in that paper, the distribution of early excess

S/N cut (σ)	n_{objects}	n_{EEEx}	Rate
N/A	127	11	$8.7 \pm 2.6\%$
3	103	11	$10.7 \pm 3.2\%$
5	92	11	$12.0 \pm 3.6\%$
8	68	11	$16.2 \pm 4.9\%$
10	49	9	$18.4 \pm 6.1\%$
15	26	5	$19.2 \pm 8.6\%$
20	18	3	$16.7 \pm 9.6\%$
30	9	2	$22 \pm 16\%$
50	4	2	$50 \pm 35\%$

Table 2. The effect on the early excess (EEEx) rate of imposing different S/N cuts on the early data, e.g. requiring that at least one epoch within five rest-frame days of inferred first light has a $>10\sigma$ detection. The two early-excess SNe that survive the 50σ cut are the two gold-tier objects (see Table 1). We quote an overall early excess rate of $12.0 \pm 3.6\%$, the value from the 5σ cut, since the rates calculated for more stringent S/N cuts are all consistent (although systematically higher) than that value.

strengths here is consistent with SNe Ia predominantly arising in single-degenerate systems.

Which rate should we quote as the single rate of early excesses in SNe Ia? As is obvious in Table 2, using a less restrictive S/N cut results in a smaller formal uncertainty due to the larger sample size, but it also means that lower intensity early excesses could be hidden in the data, undetected. We use the value calculated from the $S/N > 5$ cut, since that S/N is sufficient to detect strong early excesses, and since rates calculated with higher S/N cuts are all consistent (although systematically higher) than that value. It is possible that the higher rates derived from stricter S/N cuts are consistent with the prediction in Kasen (2010), i.e. that higher S/N data could detect weaker excesses, leading to a higher overall rate of excesses, but the uncertainties on the rates make it difficult to state

this with confidence. We thus quote the rate of early excesses in SNe Ia as $12.0 \pm 3.6\%$.

The rate of early excesses in SNe Ia which we measure here is consistent with the rate calculated in [Deckers et al. \(2022\)](#) of $18 \pm 11\%$ (calculated from the same dataset), and is also consistent with the limit of $\lesssim 30\%$ based on the non-detections in [Miller et al. \(2020b\)](#), again calculated from the same dataset. It is also consistent with the rate calculated in [Burke et al. \(2022\)](#) of $33 \pm 19\%$. [Magee et al. \(2020\)](#) find 5 excesses in a sample of 23 SNe, corresponding to a rate of $22 \pm 10\%$, which we are also consistent with. The theoretically expected rate quoted in [Kasen \(2010\)](#) is $\sim 10\%$ for strong excesses: our 5σ cut should be able to detect such excesses, and we are again consistent with this value. The rates of early excesses from all these studies, with their widely varying methodologies, are consistent with the null hypothesis that SNe Ia predominantly arise from single-degenerate systems.

Additionally, as seen in [Table 1](#), all 11 early-excess SNe are classified as normal SNe Ia. The sample contains 13 overluminous SNe Ia (i.e. 99aa-like or 91T-like), and [Jiang et al. \(2018\)](#) suggested that such overluminous SNe Ia uniformly have early excesses based on six out of six such objects in their sample exhibiting early excesses. We do not see this effect here: most of the overluminous objects in this sample do have relatively low early S/N due to their higher redshift, but two of them (ZTF18abgmcmv and ZTF18abauprj) have early S/N > 30 and still have no detectable early excess. The early-excess objects are not even clustered to the luminous end of normal SNe Ia, with only 4 of the 11 having $\Delta m_{15} < 1.0$ (as measured by `SNooPy`).

4.2. Methodology-dependent Early Excess Detections

As noted in [Section 2](#), this sample of objects was introduced in a series of three papers, and an additional paper ([Deckers et al. 2022](#)) ex-

Table 3. Which SNe in this sample have early excesses, as identified by different papers

[1]	[2]	[3]	[4]	[5]
		aapqwyv		aaqcozd
			aaqqoqs	
aavrwhu				aavrwhu
				aawjywv
				aaxsioa
			aayjvve	
				aazsabq
		abcflnz		abcflnz
		abckujq		
		abcrxoj		
			abdfazk	abdfazk
			abdfwur	
				abfhryc
		abgxvra		
				abimsyv
			abpamut	
				abssuxz
abxxssh	abxxssh	abxxssh	abxxssh	abxxssh

NOTE— The “ZTF18” has been omitted from each object name to save space. As is apparent in the table and as discussed in the text, the statement “this SN does/does not have an early excess” is methodology-dependent. References: 1: [Yao et al. \(2019\)](#), 2: [Miller et al. \(2020b\)](#), 3: [Bulla et al. \(2020\)](#), 4: [Deckers et al. \(2022\)](#), 5: this work.

amined the same dataset through the lens of Ni models. Each of these four previous studies, and now the one presented here, have independently looked for objects with early excesses. [Table 3](#) therefore lists the early-excess objects identified by each paper, each of which approached the identification with a distinct methodology: [Yao et al. \(2019\)](#) identified two early-excess objects based on photometric comparison to other objects with extremely early data (more than 17

days before peak); Miller et al. (2020b) identified zero early-excess objects, since all rising lightcurves were consistent with their general power-law fits; Bulla et al. (2020) identified six objects which had red bumps at early times in their $g - r$ color evolutions; and Deckers et al. (2022) identified six objects with early excesses, based on quantitative measures of whether they could be fit by any Ni-mixing models in the model grids from Magee et al. (2018) and Magee et al. (2020). As the table makes apparent, each paper (i.e. each methodology) identified mostly mutually exclusive sets of SNe. As stated above, we identify 11 objects with early excesses based on their fits to companion shocking models, adding another mostly-mutually-exclusive set of early-excess SNe Ia from this sample.

Even though they might seem contradictory, two things are both true: this work and each of the papers mentioned above have (different) quantitative measures to detect early excesses, and also they all mostly disagree on which objects have early excesses. These statements do not invalidate each other – we merely want to stress that even though the final cuts for which objects have early excesses can be quantitative (i.e. objective), the assumptions undergirding the methodologies introduce (subjective) biases which end up with different results.

Figures 5, 6, and 7 show the fits and residuals for three different sets of SNe drawn from the sample. Figure 5 shows the 11 objects which we identify as having an early excess, in the order of their tier as listed in Table 3. The first two objects (ZTF18aaxsioa and ZTF18abcflnz) are the two “gold” objects, because their residuals show a clear and temporally resolved shock component, manifesting as an initial discrepancy with respect to the stretch template, which then fades over time. ZTF18aaxsioa was already plotted in Figure 4, since its residuals have such a clear systematic. The next four objects (ZTF18abssuxz through ZTF18abfhryc)

are in the silver tier, since either the shock component is not as well resolved temporally (e.g. ZTF18abssuxz) or only the initial epoch or two are significantly discrepant with the stretch template. ZTF18abxxxxsh was classified as an early-excess object by most papers studying this sample (see Table 3), primarily due to its first two epochs with detections. The last five objects (ZTF18aawjyvw through ZTF18aazsabq) are in the bronze tier: their residuals don’t display systematics as obvious as the above objects, but nevertheless they are poorly fit by the stretch template alone and the models have unambiguously converged to have some shock component.

The next set of objects (Figure 6) are the eight objects which other papers identify as having an early excess, but we do not. Some objects (ZTF18aapqwyv, ZTF18aaqqqs, ZTF18abdfwur) have converged to a similar region of parameter space as SN 2019np did in Burke et al. (2022), with a large best-fit companion separation seen at a high viewing angle needed to explain the discrepancy with the stretch template – their high viewing angles have excluded them from being listed among our early-excess SNe (see the criteria listed at the start of Section 4.1). This matches the analysis of SN 2019np, where another study did identify it as having an early excess (Sai et al. 2022), even though Burke et al. (2022) did not. Others (ZTF18aayjvve, ZTF18abgxvra) have no signs of disagreement with our stretch template – in the case of ZTF18abgxvra only Bulla et al. (2020) identified it as having an early excess, and since that paper relied on color evolution to identify excesses, the object’s early peculiarities may not be obvious when looking filter-by-filter.

The last set of objects (Figure 7) was selected because the objects have exemplary early data, and also showed no signs of any early excesses (i.e. the two sets of residuals are on top of each

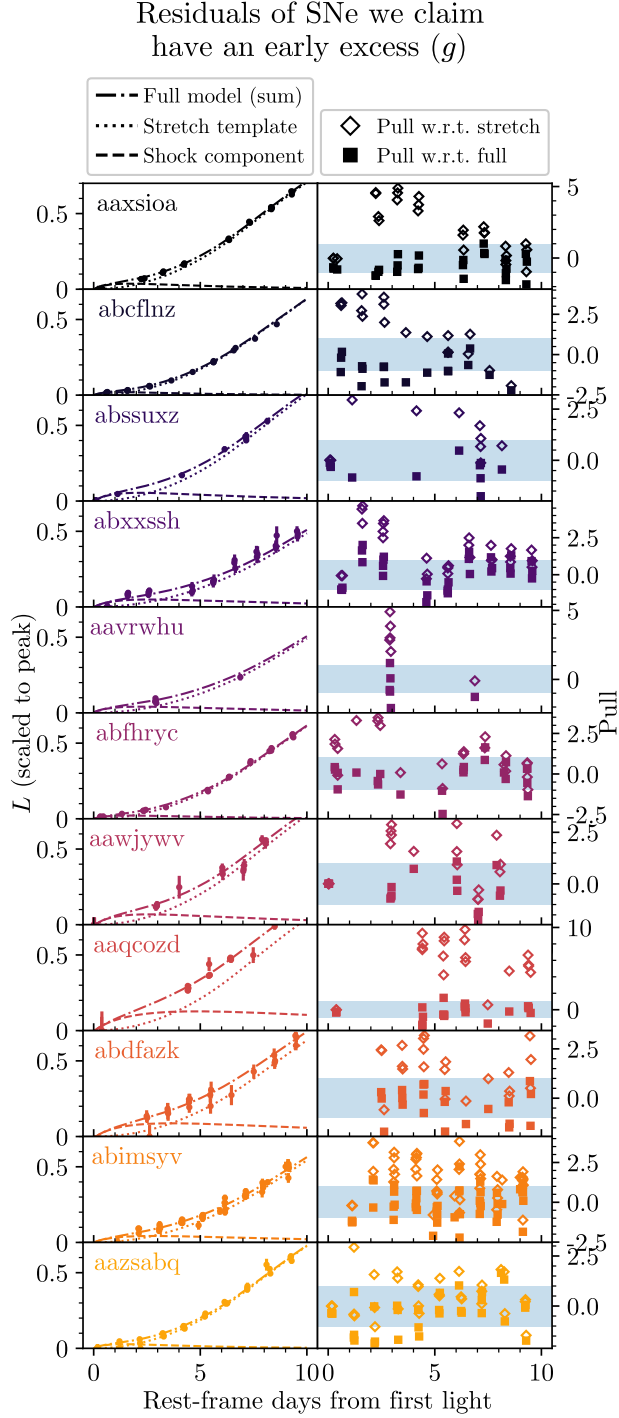


Figure 5. Fits and residuals for objects we identify as having an early excess. Objects are ordered by tier (see Table 1): the first two SNe are gold-tier (i.e. the residuals show a strong well-resolved shock component), the next four are silver-tier (the shock is not as resolved), and the last five are bronze-tier.

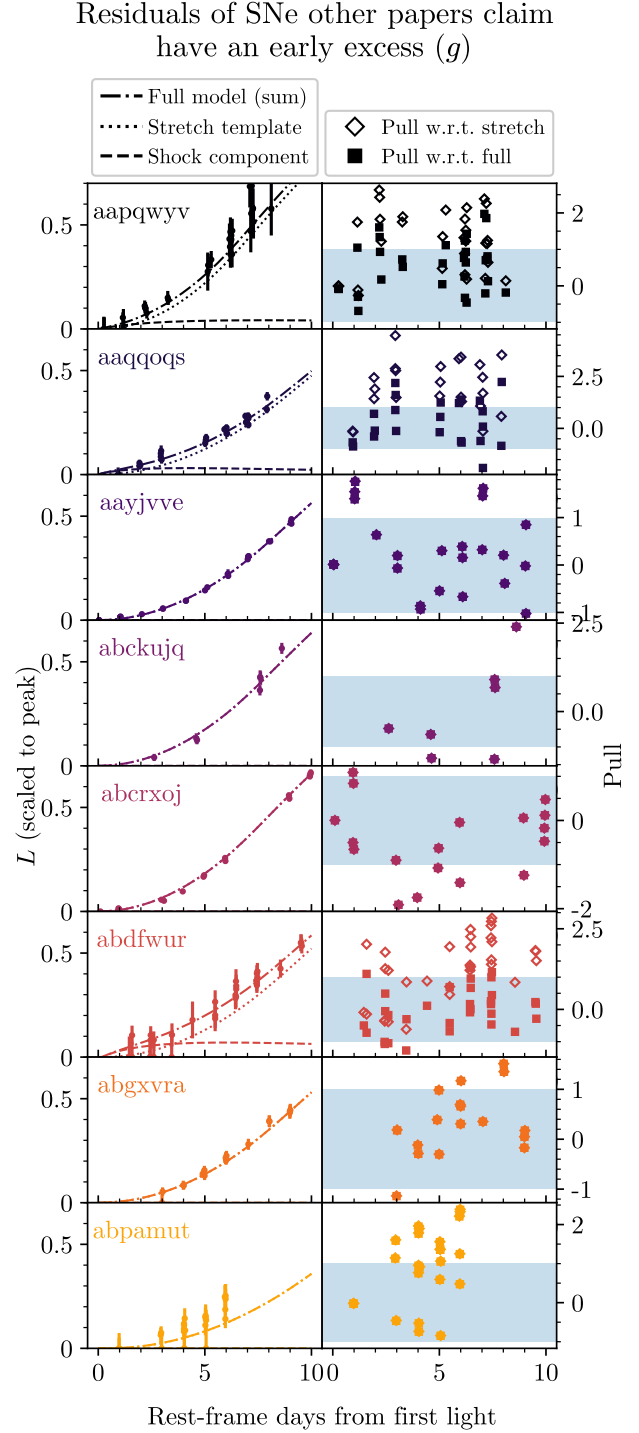


Figure 6. Identical to Figure 5, but for the objects which other papers identify as having an early excess (see Table 3). Panels are labelled with the object name, sans ZTF18-. See the text for discussion of different fits.

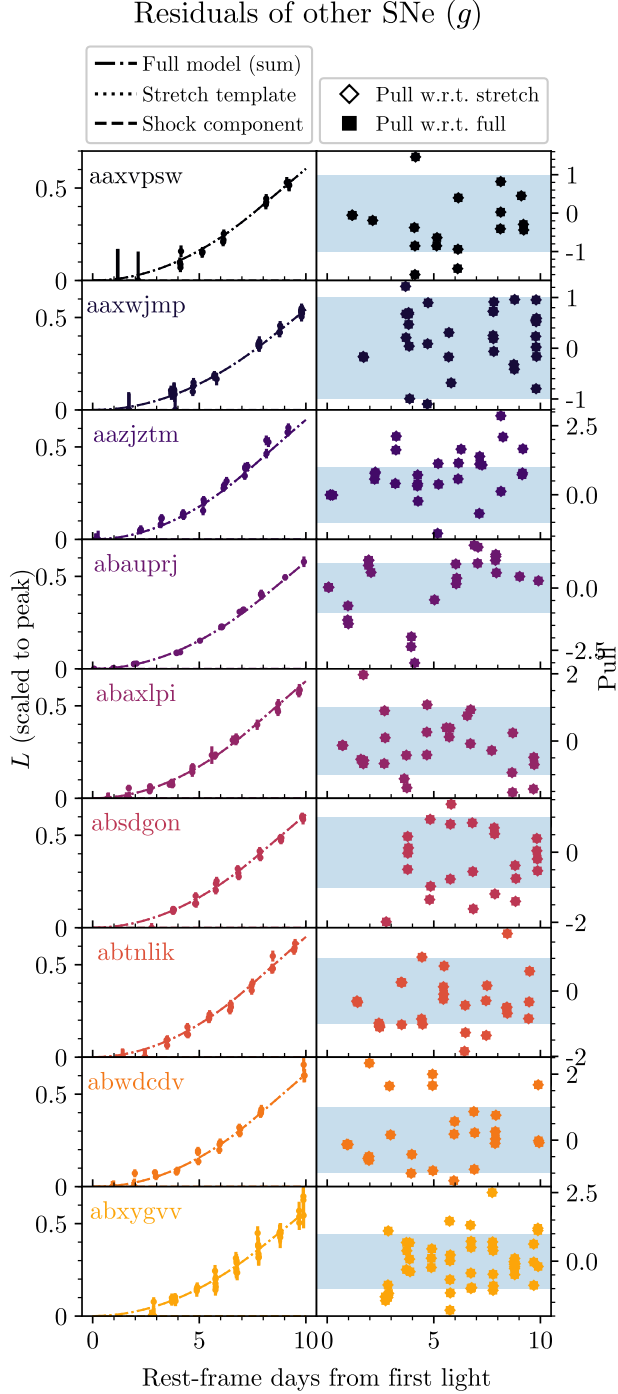


Figure 7. Identical to Figures 5 and 6, but for objects which have especially good early data, and show no signatures of an early excess. We include this figure to show that the stretch template by itself can be an excellent fit to some objects, validating its use.

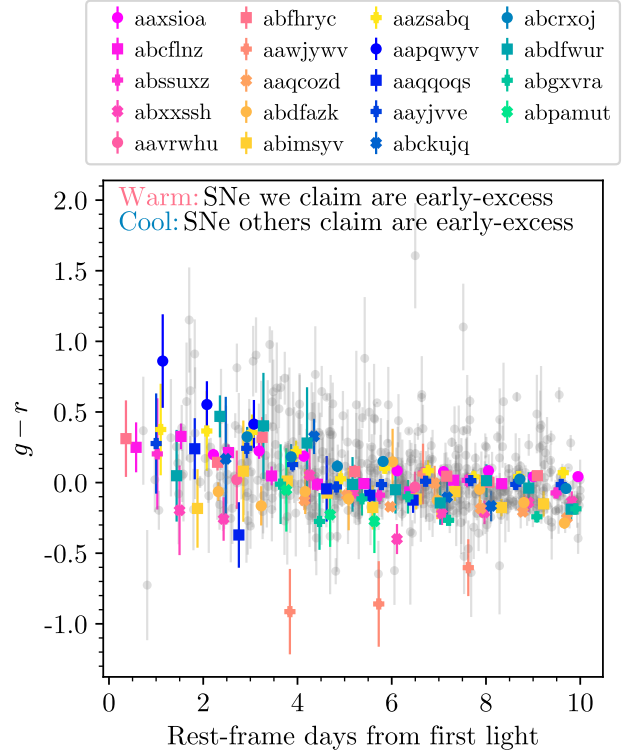


Figure 8. Color evolution of the sample. The 11 SNe we identify as having an early excess are shown in warm colors, and the 8 SNe other papers identify as having an early excess are shown in cool colors (see Table 3 for early-excess classifications). The rest of the sample is shown in grey. Colors have been extinction- and K-corrected. Compare Figures 1 and 4 of Bulla et al. (2020).

other). We include this set primarily to show that some objects have early lightcurves which are fit excellently by the stretch template alone, validating its use.

Lastly, we show the color evolution of the sample in Figure 8, highlighting early-excess objects. In Burke et al. (2022), the SN with the clearest early excess (SN 2017cbv) also had the bluest $g - r$ colors at early times. That is not quite true here, where the two SNe with the clearest early excesses in our fits (ZTF18aaxsioa and ZTF18abcflnz) are not the bluest at early times; however, ZTF18abxxssh is among the bluest SNe within three days of first light, and

it is the object that most papers identify as having an early excess (see Table 3). Generally, SNe Ia seem to show lower dispersion in their early $g - r$ evolution compared to other colors (such as $B - V$ or UV filter combinations, see Figures 9 and 10 from Burke et al. 2022), but we refer to Bulla et al. (2020) for a much more thorough investigation of this sample’s color properties.

5. CONCLUSION

We have reexamined the 2018 ZTF sample of early SNe Ia (Yao et al. 2019; Miller et al. 2020b; Bulla et al. 2020), using models from Kasen (2010) to search for signatures of nondegenerate companion interaction in the form of early excesses in the lightcurves. We found 11 such objects with signatures of companion interaction: this naïvely represents 8.7% of the sample, but when compensating for the S/N of the early data we calculate an overall early excess rate of $12.0 \pm 3.6\%$. This rate is consistent with several others calculated throughout the literature, using different methodologies and/or samples to detect early excesses. This rate is also consistent with the expectation that SNe Ia predominantly arise from progenitor systems with a Roche-lobe-overflowing nondegenerate companion. However, early excesses only occur in this sample in normal SNe Ia and not in any of the 13 overluminous objects, which is inconsistent with the claim in Jiang et al. (2018) that overluminous SNe Ia have ubiquitous early excesses.

In addition to this result, we also showed that the detection of early excesses can be methodology-dependent. For instance, despite the fact that this same sample had been analyzed by four previous papers, each of which looked for objects with early excesses, we iden-

tify seven SNe Ia as having early excesses which none of the previous papers identified as such. This meta-analysis shows that different methodologies make a variety of assumptions about the early lightcurves of SNe Ia, which can lead to different results.

Companion interaction models have been shown for several years to be excellent (if imperfect) fits to SNe Ia with early excesses (see e.g. Hosseinzadeh et al. 2017; Dimitriadis et al. 2019; Burke et al. 2021; Hosseinzadeh et al. 2022; Burke et al. 2022). We strongly encourage the observation of large samples of SNe Ia with high-cadence multiwavelength early data (such as the ones in this paper and in Burke et al. 2022) so that models’ predictions might be tested and the uncertainty around the progenitor systems of SNe Ia might be gradually reduced. We also encourage continued theoretical work on companion interaction models, since the state of the art is now more than a decade old (Kasen 2010).

J.B. and D.A.H. are supported by NSF grants AST-1911151 and AST-1911225, as well as by NASA grant 80NSSC19kf1639.

Time domain research by D.J.S. and G.H. is supported by NSF grants AST-1821987, 1813466, 1908972, & 2108032, and by the Heising-Simons Foundation under grant #2020-1864.

Facilities: Zwicky Transient Facility (Bellm et al. 2019)

Software: `astropy` (Astropy Collaboration et al. 2013; The Astropy Collaboration et al. 2018), `SNOOPY` (Burns et al. 2011), `lightcurve_fitting` (Hosseinzadeh 2019), `emcee` (Foreman-Mackey et al. 2013), `extinction` (Barbary 2016)

REFERENCES

- Ashall, C., Lu, J., Shappee, B. J., et al. 2022, ApJL, 932, L2
- Astropy Collaboration, Robitaille, T. P., Tollerud, E. J., et al. 2013, A&A, 558, A33

- Barbary, K. 2016, Extinction V0.3.0, Zenodo, Zenodo, doi:10.5281/zenodo.804967
- Bellm, E. C., Kulkarni, S. R., Graham, M. J., et al. 2019, *PASP*, 131, 018002
- Botyánszki, J., Kasen, D., & Plewa, T. 2018, *ApJL*, 852, L6
- Brown, P. J., Dawson, K. S., Harris, D. W., et al. 2012, *ApJ*, 749, 18
- Bulla, M., Miller, A. A., Yao, Y., et al. 2020, *ApJ*, 902, 48
- Burke, J., Howell, D. A., Sarbadhicary, S. K., et al. 2021, *ApJ*, 919, 142
- Burke, J., Howell, D. A., Sand, D. J., et al. 2022, arXiv e-prints, arXiv:2207.07681
- Burns, C. R., Stritzinger, M., Phillips, M. M., et al. 2011, *AJ*, 141, 19
- Cao, Y., Kulkarni, S. R., Howell, D. A., et al. 2015, *Natur*, 521, 328
- Conley, A., Sullivan, M., Hsiao, E. Y., et al. 2008, *ApJ*, 681, 482
- Deckers, M., Maguire, K., Magee, M. R., et al. 2022, *MNRAS*, 512, 1317
- Dessart, L., Leonard, D. C., & Prieto, J. L. 2020, *A&A*, 638, A80
- Dimitriadis, G., Foley, R. J., Rest, A., et al. 2019, *ApJL*, 870, L1
- Foreman-Mackey, D., Hogg, D. W., Lang, D., & Goodman, J. 2013, *PASP*, 125, 306
- Gehrels, N., Chincarini, G., Giommi, P., et al. 2004, *ApJ*, 611, 1005
- Hosseinzadeh, G. 2019, Light Curve Fitting, vv0.0.0, Zenodo, doi:10.5281/zenodo.2639464. <https://doi.org/10.5281/zenodo.2639464>
- Hosseinzadeh, G., Sand, D. J., Valenti, S., et al. 2017, *ApJL*, 845, L11
- Hosseinzadeh, G., Sand, D. J., Lundqvist, P., et al. 2022, arXiv e-prints, arXiv:2205.02236
- Hoyle, F., & Fowler, W. A. 1960, *ApJ*, 132, 565
- Iben, I., J., & Tutukov, A. V. 1984, *ApJS*, 54, 335
- Jiang, J.-a., Doi, M., Maeda, K., & Shigeyama, T. 2018, *ApJ*, 865, 149
- Jiang, J.-A., Doi, M., Maeda, K., et al. 2017, *Nature*, 550, 80
- Jiang, J.-a., Maeda, K., Kawabata, M., et al. 2021, *ApJL*, 923, L8
- Kasen, D. 2010, *ApJ*, 708, 1025
- Khokhlov, A. M. 1991, *A&A*, 245, 114
- Li, W., Wang, X., Vinkó, J., et al. 2019, *ApJ*, 870, 12
- Magee, M. R., & Maguire, K. 2020, *A&A*, 642, A189
- Magee, M. R., Maguire, K., Kotak, R., et al. 2020, *A&A*, 634, A37
- Magee, M. R., Sim, S. A., Kotak, R., & Kerzendorf, W. E. 2018, *A&A*, 614, A115
- Marion, G. H., Brown, P. J., Vinkó, J., et al. 2016, *ApJ*, 820, 92
- Miller, A. A., Cao, Y., Piro, A. L., et al. 2018, *ApJ*, 852, 100
- Miller, A. A., Magee, M. R., Polin, A., et al. 2020a, *ApJ*, 898, 56
- Miller, A. A., Yao, Y., Bulla, M., et al. 2020b, *ApJ*, 902, 47
- Ni, Y. Q., Moon, D.-S., Drout, M. R., et al. 2022a, *Nature Astronomy*, arXiv:2202.08889
- . 2022b, arXiv e-prints, arXiv:2206.12437
- Pankey, Titus, J. 1962, PhD thesis, Howard University, Washington DC
- Perlmutter, S., Aldering, G., Goldhaber, G., et al. 1999, *ApJ*, 517, 565
- Phillips, M. M., Lira, P., Suntzeff, N. B., et al. 1999, *AJ*, 118, 1766
- Piro, A. L., & Nakar, E. 2013, *ApJ*, 769, 67
- Polin, A., Nugent, P., & Kasen, D. 2019, *ApJ*, 873, 84
- Riess, A. G., Filippenko, A. V., Challis, P., et al. 1998, *The Astronomical Journal*, 116, 1009–1038. <http://dx.doi.org/10.1086/300499>
- Sai, H., Wang, X., Elias-Rosa, N., et al. 2022, *MNRAS*, 514, 3541
- Sand, D. J., Amaro, R. C., Moe, M., et al. 2019, *ApJL*, 877, L4
- Schlafly, E. F., & Finkbeiner, D. P. 2011, *ApJ*, 737, 103
- Schlegel, D. J., Finkbeiner, D. P., & Davis, M. 1998, *ApJ*, 500, 525
- Shappee, B. J., Holoién, T. W. S., Drout, M. R., et al. 2019, *ApJ*, 870, 13
- Shen, K. J., Blondin, S., Kasen, D., et al. 2021, *ApJL*, 909, L18
- Siebert, M. R., Dimitriadis, G., Polin, A., & Foley, R. J. 2020, *ApJL*, 900, L27
- Sim, S. A., Fink, M., Kromer, M., et al. 2012, *MNRAS*, 420, 3003
- Taubenberger, S. 2017, in *Handbook of Supernovae*, ed. A. W. Alsabti & P. Murdin (Springer, Cham)

The Astropy Collaboration, Price-Whelan, A. M.,
Sipőcz, B. M., et al. 2018, ArXiv e-prints,
arXiv:1801.02634
Tucker, M. A., Shappee, B. J., Valley, P. J., et al.
2020, MNRAS, 493, 1044

Tucker, M. A., Ashall, C., Shappee, B. J., et al.
2021, ApJ, 914, 50
Yao, Y., Miller, A. A., Kulkarni, S. R., et al. 2019,
ApJ, 886, 152